Effects of Solar Photovoltaic Panels on Roof Heat Transfer

Anthony Dominguez[a], Jan Kleissl[a], and Jeffrey C. Luvall[b]

[a]*University of California, San Diego, Department of Mechanical and Aerospace Engineering*

[b]*NASA, Marshall Space Flight Center, AL 35812, USA*

Corresponding author
Jan Kleissl, jkleissl@ucsd.edu
Office: (858) 534-8087; Fax: (858) 534-7599;
Address: 9500 Gilman Dr, EBUII – 580, University of California, San Diego, La Jolla, CA, 92093-0411

Abstract

Indirect benefits of rooftop photovoltaic (PV) systems for building insulation are quantified through measurements and modeling. Measurements of the thermal conditions throughout a roof profile on a building partially covered by solar photovoltaic (PV) panels were conducted in San Diego, California. Thermal infrared imagery on a clear April day demonstrated that daytime ceiling temperatures under the PV arrays were up to 2.5 K cooler than under the exposed roof. Heat flux modeling showed a significant reduction in daytime roof heat flux under the PV array. At night the conditions reversed and the ceiling under the PV arrays was warmer than for the exposed roof indicating insulating properties of PV. Simulations showed no benefit (but also no disadvantage) of the PV covered roof for the annual heating load, but a 5.9 kWh m^{-2} (or 38%) reduction in annual cooling load. The reduced daily variability in rooftop surface temperature under the PV array reduces thermal stresses on the roof and leads to energy savings and/or human comfort benefits especially for rooftop PV on older warehouse buildings.

Keywords: Building energy use; cooling load; photovoltaic; roof heat flux; thermal infrared camera

1. Introduction

Building Heating, Ventilation and Air Conditioning (HVAC) is a major contributor to urban energy use. Especially in poorly insulated, single story buildings with large surface area such as warehouses, most of the heat enters through the roof. Increasing roof albedo (or solar reflectance) reduces cooling load in sunny and hot climates. Installing reflective roof membranes resulted in seasonal air-conditioning energy savings of 57% on a California home (Akbari et al., 1997a), 49% on a bungalow, 2% to 43% in Florida (Parker and Parkaszi, 1997) , and 30 Wh m^{-2} d^{-1} on a regeneration building (Akbari and Rainer, 2000). However, the energy savings depend on the roof insulating properties. Increasing the roof albedo from 0.09 to 0.75 on a building without insulation resulted in energy savings of 28%, while increasing the albedo from 0.30 to 0.75 on a building with R-30 insulation (an addition of 5.28 K m^2 W^{-1} in thermal resistance) resulted in savings of only 5% (Simpson and McPherson, 1997).

Shade trees planted near residential buildings resulted in a seasonal cooling energy savings of 30% and peak demand savings of 27% and 42% in two Sacramento, CA residences (Akbari et al., 1997b).

A rooftop 'modification' whose impact on cooling loads has not been examined experimentally is solar photovoltaic (PV) arrays. In California alone, over a GW (10^9 Watts, corresponding to about 1 km^2 of rooftop space) in residential and commercial rooftop PV are approved or in the planning stages. An indication of the influence of PV on cooling comes from an evaluation of residential building energy use at 260 sites in southern California pre and post installation of a PV system, which indicated that AC energy use in high cooling degree day conditions decreased compared to a reference sample (ITRON Inc., 2010). A 1 degree increase in daily average

temperature in San Diego Gas & Electric (SDG&E) territory caused post-PV households with air conditioning to use 0.501 kWh less energy per day than households with air conditioning that did not have PV installed.

Modeling the effects of building integrated PV (BIPV) on the microclimate of the urban canopy layer showed a significant reduction in BIPV roof surface temperatures compared to a conventional roof with albedo 0.30 and a thermal resistance of 1.33 K m^2 W^{-1} (Tian et al., 2007). A one dimensional transient heat transfer model showed a peak cooling load savings of 52% with ventilated BIPV compared to traditional roofing with a solar absorbance of 0.9 and a thermal resistance of 1.33 K m^2 W^{-1} (Wang et al., 2006). A conduction model showed a 65% reduction in cooling load component through a PV roof compared to a conventional roof with a thermal resistance of 2.8 K m^2 W^{-1} (Yang et al., 2001).

In this study, we investigate a building partially covered by a flush and horizontal solar PV array and an offset and tilted solar PV array (Section 2). Meteorological and roof temperature measurements (including thermal imagery) were conducted (Section 3). Section 4 describes a roof conduction model to estimate average and peak cooling energy differences for the roof sections with and without PV. In Section 5 we present a full roof energy balance model to calculate annual roof heating and cooling loads with and without PV. Conclusions are presented in section 6.

2. Experimental setup

2.1. Building and location

The building used in this study is the Powell Structural Laboratory (PoSL) at the University of California, San Diego (Fig. 1; Tables 1,2). It is a hollow concrete cube without HVAC system. There are no windows except for a small partially shaded row of windows on the east and west sides near the roof. On workdays the building is cooled by natural ventilation through a gate on the south face of the building (many coastal buildings in San Diego lack HVAC systems as the sea breezes keep the indoor environment comfortable for most of the year). Due to safety and productivity considerations, the experiment had to be conducted on a weekend day, when all doors were closed and the building was 'ventilated' only through infiltration. PoSL has 2 solar PV arrays on the rooftop; one is tilted south at 4.4 degrees and elevated 0.10 m off of the roof surface and the other is horizontal and flush with the roof surface (Fig. 2). The roof is 0.20 m thick and composed of mesh reinforced insulating concrete and 24 GA corrugated steel on top of trusses. This results in a significantly lower R-Value than new construction, but is typical of older warehouse buildings with large, flat rooftops for which PV is an attractive option. Table 1 shows the site and building characteristics.

Table 1: Powell Structural Laboratory (PoSL) building characteristics. The building is located at 32 ^{o}52'50"N, 117^{o}14'06"W in the World Geodetic System 1984 coordinate system (WGS84) and is 1.7 km from the Pacific Ocean coastline.

Length (north-south)	Width (east-west)	Height	Rooftop area	Measured Roof Albedo
36.6 m	19.2 m	18.0 m	703 m^2	0.218

Table 2: PoSL flush PV array characteristics (see also Fig. 1c). The tilted PV array is identical to the flush array with the exception of the 4.4 degree south tilt (measured average of 14 panels

on the edge of the array) and a length of 6.99 m. The total rated DC output is 13 kW (200 W per panel).

Length	Width	# of panels	Panel Type	Solar Reflectance	Solar Conversion Efficiency
6.01 m	7.80 m	8X4 = 32	Kyocera	0.178	0.08

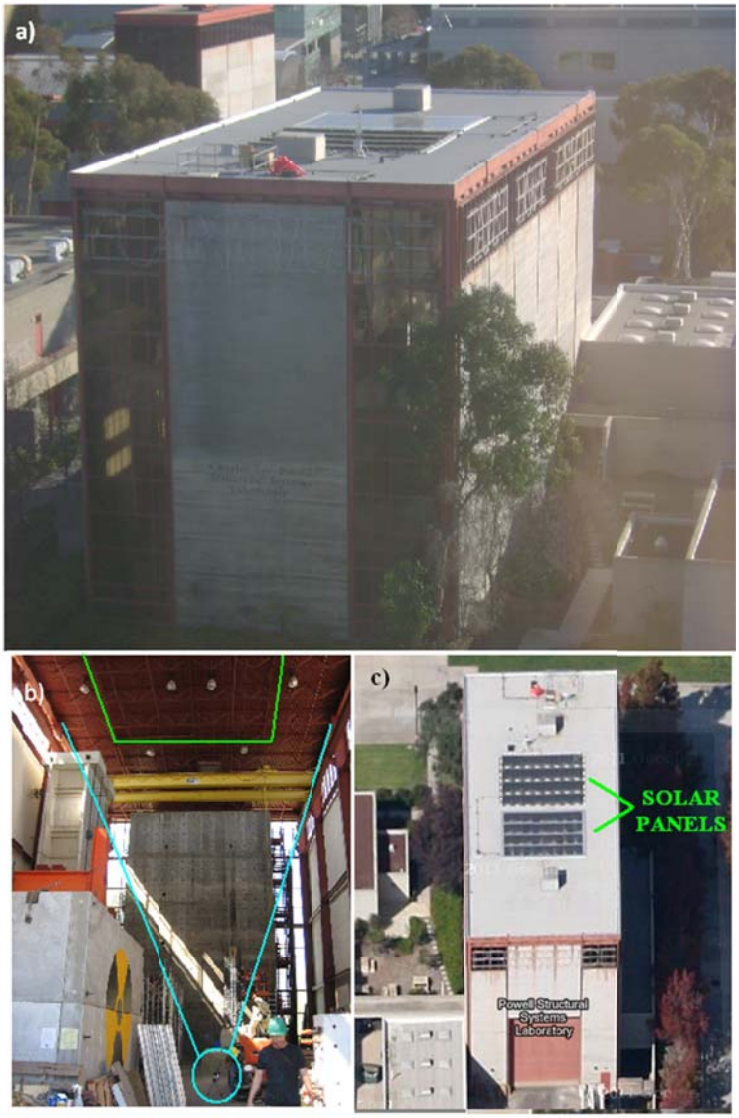

Fig. 1. a. Photograph of PoSL facing South; b. Photograph of PoSL from inside facing North with TIR camera circled, field of view shown by blue lines, and PV location outlined in green; c. Google Earth image of PoSL (North is up) with tilted array on the North side of the roof and

flush array in the center. The larger North-South panel spacing makes the tilted array appear larger (Table 2).

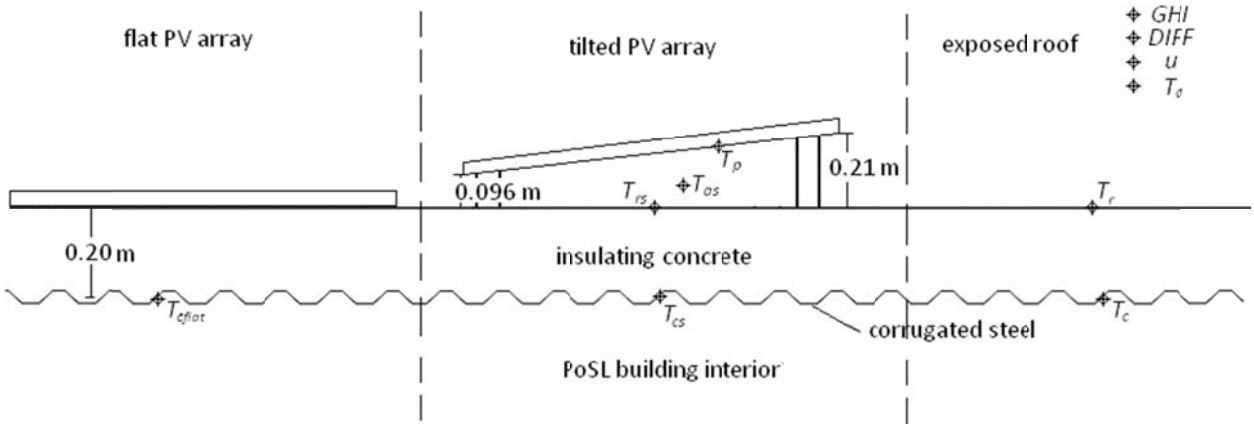

Fig. 2. South (left) to North (right) vertical cross-section of the PoSL roof (to scale except for discontinuities at the vertical dashed lines) with schematic of all exterior measurements (for variable definitions see Table 3). The PV panels are 1.4 m long. The tilted PV panels are raised allowing airflow between panel and roof, while the flat panels are flush to the roof surface. The ceiling temperatures T_c , T_{cs} and T_{cflat} are representative of different areas within the TIR camera image (Fig. 3).

2.2. Equipment

2.2.1. Interior measurements

Data were taken from 1500 PST Friday, April 17, 2009 to 0600 PST Monday, April 20, 2009. Inside the building, a FLIR A320 thermal infrared (TIR) camera with a 45^{o} wide angle lens was pointed at the ceiling to record the longwave irradiance (Fig. 1b). Since even the wide angle view was not sufficient to capture the entire ceiling, the TIR camera was positioned to image partially the ceiling under the flush array and the exposed part of the roof, and the full area

under the tilted array (Fig. 3). TIR images containing 320x240 pixels were taken every 5 minutes throughout the study period. The surface temperature of each pixel was computed using Stefan's law assuming an emissivity of 0.95. This assumption was verified by comparing TIR temperatures to that of a contact thermocouple sensor affixed to the ceiling with heat conducting epoxy.

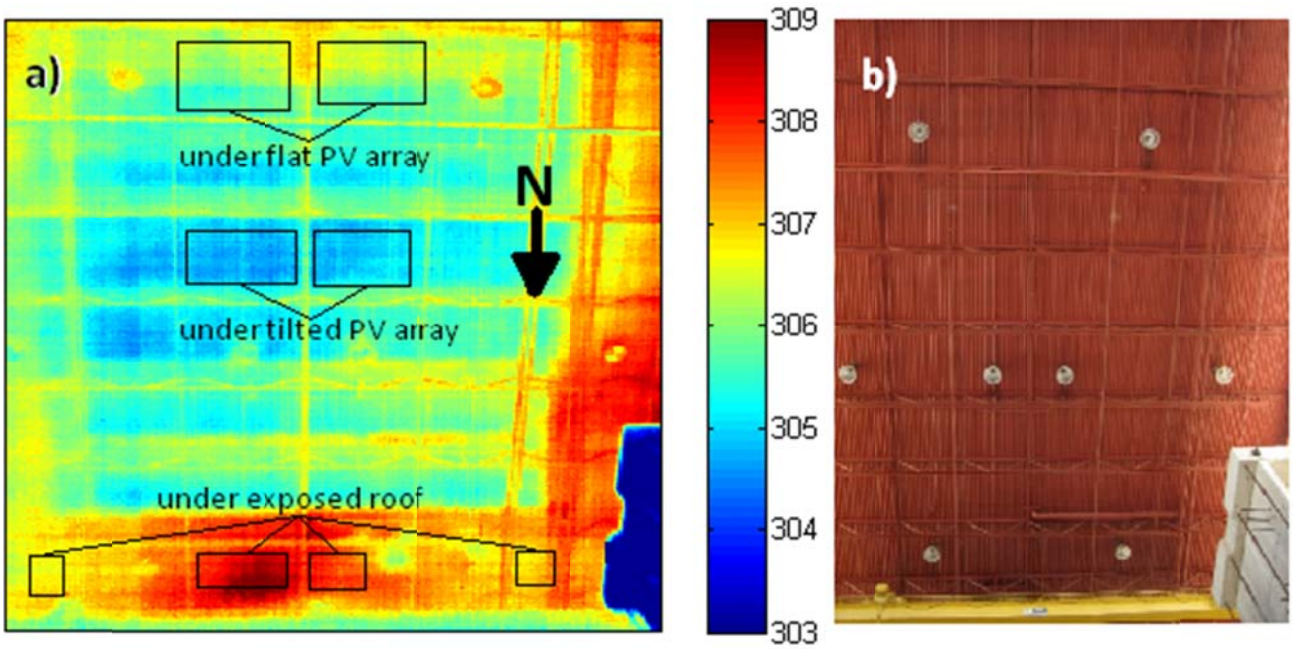

Fig. 3. a. Thermal IR camera image of ceiling at 1710 PST on April 19, 2009. The color bar denotes temperature in K. Horizontal and vertical lines through the image result from steel trusses that are below the ceiling at a different temperature. The footprint of the tilted PV array is visible as a cool area in the center. Pixels within black rectangles were chosen as representative of the ceiling underneath each roof type and were used to obtain its average temperature. b. Photograph of the ceiling from same angle. The cooler (turned off) lamps on the ceiling provide landmarks to visually georeference the images.

2.2.2. Exterior measurements

Surface temperature was measured by affixing HOBO ProV2 external temperature sensors using heat conducting epoxy to both the underside of the tilted solar panels and the surface of the roof under the solar panel (Fig. 2). An air temperature probe was mounted 0.1 m above the roof surface under the tilted array. The space under the flush array was inaccessible so no measurements could be taken there. The sampling frequency was 1-min and 5-min averages were stored.

A permanent meteorological station on the rooftop of PoSL monitored exposed roof surface temperature, air temperature, total and diffuse solar irradiance, and wind speed (Table 3). Data were sampled every second and stored as 5-min averages. The rooftop albedo and solar PV albedo were measured using a Kipp & Zonen CMP3 albedometer. After the study, the TIR camera, HOBOs, and TN9 TIR sensors were cross-calibrated on the exposed roof and a linear regression was applied to force agreement between the sensors. Appendix A shows an analysis of the sensitivity of our results to temperature offsets in the sensors.

Table 3: Sensor type, make, model, and height above roof level (ARL) for measurements on the PoSL roof (Fig. 2). The TN9 accuracy is given for the 15-35^{o}C temperature range. Full range accuracy is 2^{o}C.

Measurement	**Variable**	**Sensor**	**Height**	**Accuracy**
Roof surface temperature	T_r	ZyTemp TN9 TIR	1.41 m	0.6 ^{o}C
Air temperature	T_a	Sensirion SHT75 T/RH	1.93 m	0.4 ^{o}C
Global horizontal incident solar	*GHI*	LiCor SZ200 pyranometer	2.26 m	3%

irradiance				
Diffuse horizontal solar irradiance	*DIFF*	Dynamax SPN1 pyranometer	2.27 m	5%
Wind speed	*u*	Davis wind sensor	2.00 m	5%
Temperatures under tilted PV array:				
Roof surface temperature	T_{rs}	Hobo ProV2	0.0 m	0.2 ^{o}C
Air temperature under tilted array	T_{as}	Hobo ProV2	0.1 m	0.2 ^{o}C
PV backpanel temperature	T_{p}	Hobo ProV2	0.17 m	0.2 ^{o}C

3. Measurement results

3.1. Solar radiation, wind speed, and outside air temperature

Only data for Sunday, April 19, 2009 are analyzed, because it was the clearest day with a few clouds from 0730 to 1000 PST (Fig. 4a). The daily global horizontal solar irradiation was 7.72 kWh m^{-2}, which was larger than a typical April day. Figure 4b shows the wind speed, which follows typical sea breeze patterns (cf. annual average *u* in Fig. 4b) with calm winds until 0800 PST, increases to 5 m s^{-1} at 1400 PST and decreases to less than 1 m s^{-1} by 2030 PST. The air temperature cycle (Fig. 5a) has a small diurnal amplitude. Overall the meteorological conditions on April 19 were representative for coastal southern California where much of the growth in PV is expected to occur.

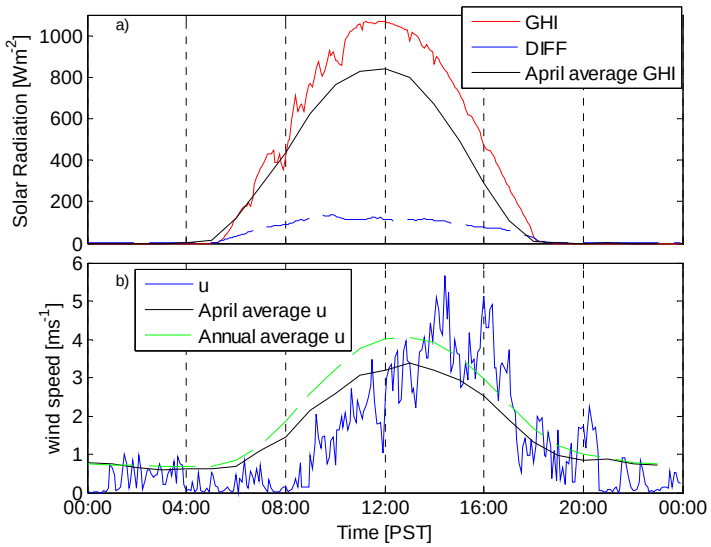

Fig. 4. a. Diffuse and global horizontal incident solar irradiance and b. wind speed on April 19, 2009 (see Table 3 for details on sensors and measurement locations).

3.2. Roof and ceiling temperatures

Figure 5a shows the temperatures of outside air, roof, and ceiling for the exposed roof. The roof surface temperature peaks at noon and is higher than the air and ceiling surface temperatures during daylight hours, as it is heated directly by solar radiation. The ceiling surface temperature peaks at 1737 PST due to a time lag in the transport of heat from the exterior roof surface to the interior ceiling surface.

Figure 5b shows the temperatures under the tilted PV array. The back panel temperature of the solar panel is similar to the roof temperature for the exposed roof. However, since the roof surface underneath the PV panel is shaded its temperature is significantly lower than for the exposed roof. The air temperature in the gap between the panel and the roof is lower than the back panel temperature and roof temperature under the panels, but higher than the air temperature at 1.93 m above the roof. To conclude the roof under the solar panels is heated by

longwave radiation from the panel underside and diffuse radiation from the sky (which is small given the small tilt angle), the sum of which is less than the solar irradiance to the exposed roof. Convection of air through the air space below the panel results in heat removal. At night, the roof surface under the solar panels remains warmer, due to the reduction in radiative cooling to the sky.

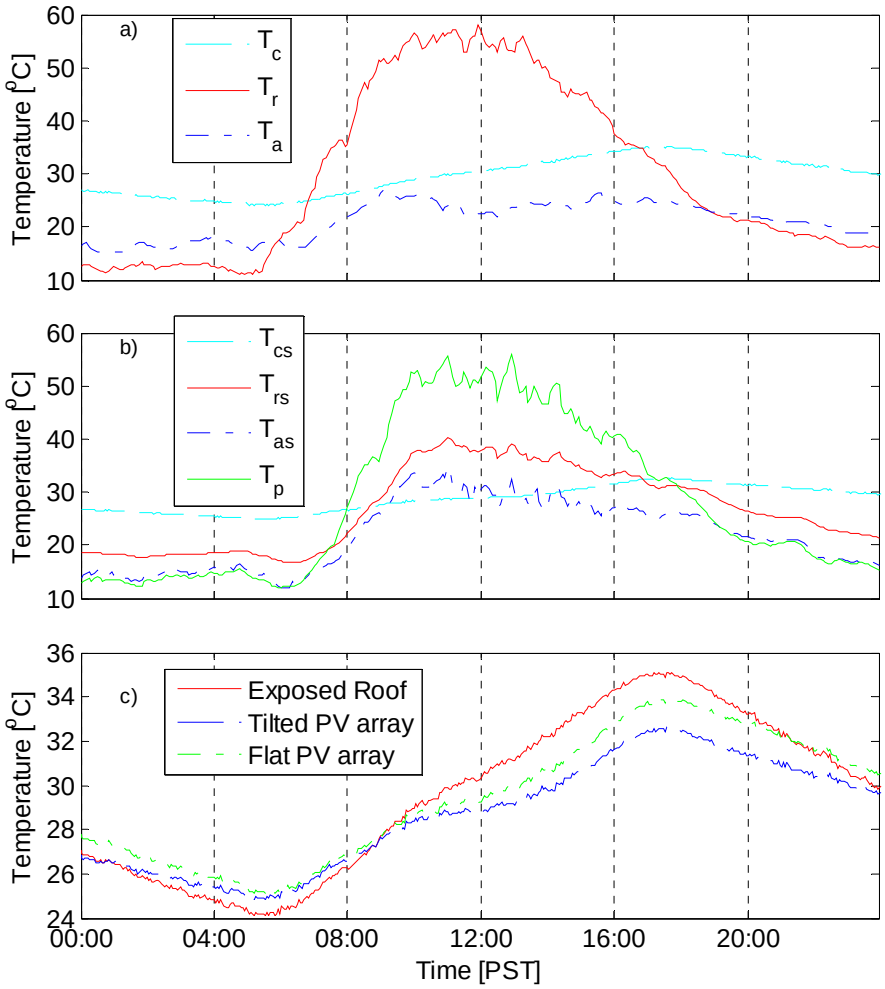

Fig. 5. a. Ceiling surface (T_c), roof surface (T_r) and outside air temperature (T_a) measurements for the exposed roof. b. Ceiling surface (T_{cs}), roof surface (T_{rs}), outside air (T_{as}), and back panel temperature (T_p), measurements under the tilted PV array. c. Interior ceiling surface

temperatures under exposed roof, tilted PV array, and flat PV array averaged over areas identified in Fig. 3.

The interior ceiling surface temperatures (below the exposed roof, tilted PV array, and flush PV array) are redrawn for clarity in Figure 5c. From 0900 to 2100 PST the ceiling under the exposed roof is warmer than the ceiling underneath the flush panels, which in turn is warmer than the ceiling underneath the tilted panels. The maximum temperature difference between exposed roof and tilted PV is 2.5 ^{o}C at 1700 PST. The temperature of the ceiling underneath the flush PV array is between the other cases during the daytime, as it provides shading to the roof, but the enclosed airspace between the panels and the roof limits horizontal advection of heat. The ceiling covered by the flush PV array has the highest temperature at night due to the insulating properties of the enclosed air between roof and solar array and the increase in incident longwave radiation from the panel compared to the sky.

4. Simulation of roof heat flux

The results in section 3 have shown marked differences in the thermal response of a roof underneath a solar panel compared to that of an exposed roof. However, to determine the potential HVAC energy savings associated with solar PV panels the roof heat flux into the air conditioned space (or roof cooling load) is the most relevant variable. Quantifying this heat flux independently for each surface is difficult, since convective and radiative (and to a lesser extent conductive) exchange of heat between ceiling areas through the room air and wall and floor surfaces blunts the true differences between the ceiling temperatures under each roof type.

The conduction heat flux through the roof can be modeled using a Crank-Nicholson method (Underwood and Yik, 2004) applied to the one-dimensional transient heat conduction equation

$$\rho c_p \frac{\partial T}{\partial t} = k \frac{\partial^2 T}{\partial x^2} \quad (1)$$

using a discretization of 32 layers. The boundary conditions are the measured rooftop surface and interior ceiling surface temperatures. The effects of the upper roof membrane and lower corrugated steel (Fig. 2) were negligible, as they are thin and have high thermal conductivity in comparison to the insulating concrete, so the model was simplified by defining the entire roof as mesh reinforced insulating concrete. The thermal properties used in the model were thermal conductivity k = 0.38 W m^{-1} K^{-1}, density ρ = 1200 kg m^{-3}, and heat capacity c_p = 1000 J kg^{-1} K^{-1} (Thermal Properties of Concrete, 2010), resulting in a thermal diffusivity of 3.2 x 10^{-7} m^2 s^{-1} and thermal resistance of 0.526 K m^2 W^{-1}(about the equivalent of R-3 insulation). The model was validated against an analytical solution for a block with uniform initial temperature being submerged into a liquid with constant uniform temperature (Underwood and Yik, 2004). Since the system is quasi-periodic on clear days, the initial temperature profile in the roof was estimated by taking the temperature profile at the end of the day and adding a linear fit so that the surface temperatures match the initial measured surface temperatures.

From the modeled roof temperature profile a time lag in heat penetration from rooftop to ceiling is apparent (Fig. 6). For the exposed roof, the cooling and heating of the upper surface drives the heat conduction through the roof (Fig. 6a). Under the tilted PV array however, while heating from the top is dominant, heating from the bottom also occurs (Fig. 6b). Though the interior air temperature was not measured, the underside of a concrete block surface within the building captured by the TIR camera (bottom right of Fig. 3a) was significantly larger than

the outside air temperature and typical temperature for air conditioned buildings. The fact that building is not ventilated or air conditioned leads to an increase in indoor air temperature and reduction in roof heat flux.

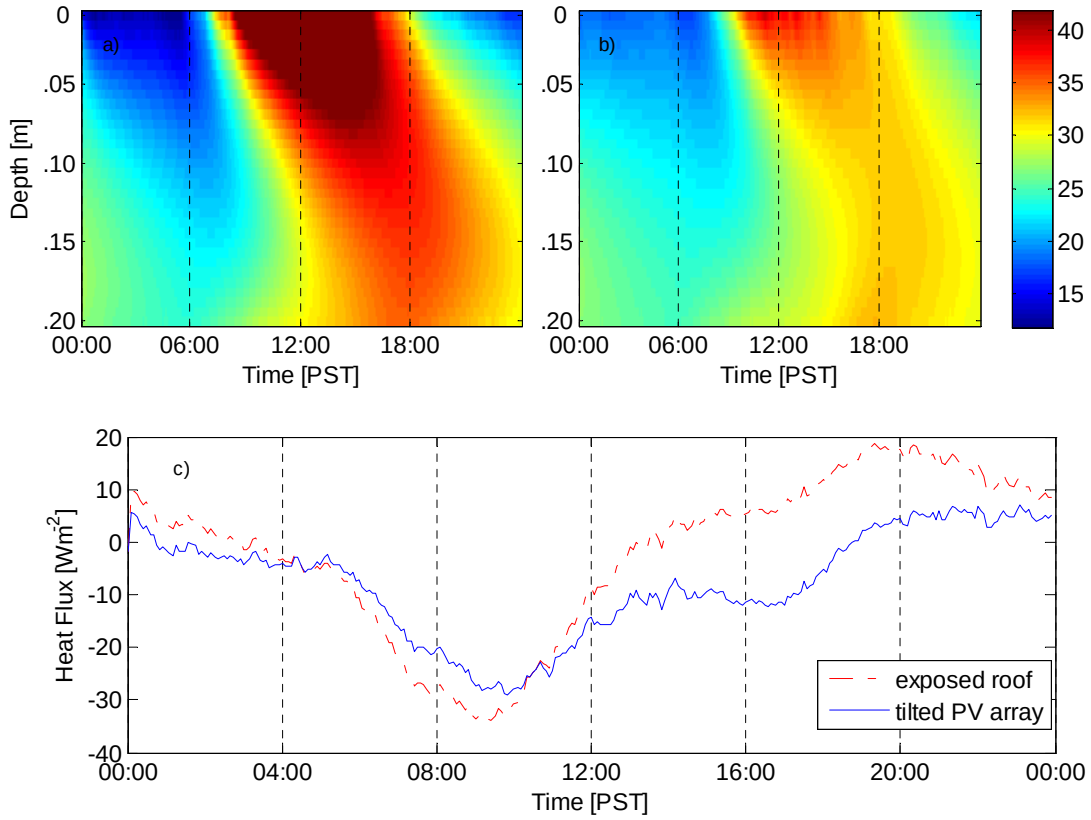

Fig. 6. Time series of simulated 1-D temperature profile through a. the exposed roof and b. the roof under the tilted PV array. The color bar shows temperature in ^{o}C. c. Conductive heat flux from bottom roof layer to ceiling surface for the exposed roof and the tilted PV array (negative means upward flux as per Eq. 2).

Given the energy balance at the ceiling, the heat flux into the indoor building air (or roof cooling load) should be equal to the conductive heat flux into the bottom roof layer (layer 32)

$$q = \frac{k}{\Delta x}\left(T_{31} - T_{32}\right), \qquad (2)$$

where Δx is the numerical discretization distance between roof layers. This analysis cannot be conducted for the flush PV array as the exterior roof temperature was not available to drive the conduction model. Appendix B shows an attempt to estimate the flush array heat flux.

Figure 6c shows the resulting heat flux through the exposed roof and the roof under the tilted array. As expected the heat flux is negative (upward) in the early morning. The minimum between 0900-1000 PST is a result of the heat loss at the roof surface through the night but likely amplified by solar radiative heating of the interior and ceiling through the windows in the early morning as well as increased convective heating from the interior air temperature. At 1300 PST (exposed roof) and 1900 PST (tilted PV) the heat flux becomes positive (downward) with a larger peak for the exposed roof than the PV covered roof at 1930 PST. The heat fluxes remain positive through the night consistent with the time lag of heat transfer through the roof. Generally, the relatively small thermal diffusivity of the roof under consideration causes secondary effects (ceiling-building interaction, window shortwave transmission) to have a significant influence on the modeled conductive heat fluxes near the ceiling.

5. Modeling annual roof heat flux

5.1. Roof heat flux

Table 4: Variables used in the annual roof heat flux model and their sources.

Term	Description	Source
a	Velocity coefficient in h_c for exposed roof/PV covered roof	18.65/14.82 (Palyvos, 2008)
b	Velocity exponent in h_c for exposed roof/PV covered roof	0.605/0.420 (Palyvos, 2008)
h_c	Exterior convective heat transfer coefficient	DOE -2 model (Eq. 9)
h_i	Interior convective heat transfer coefficient	1.25 W m^{-2} K^{-1} (ASHRAE 2005b)
SVF	Skyview factor of roof under PV panel	0.0817 (Calculated from panel angle)

u	Wind speed	Measured 2 m ARL
DIFF	Diffuse irradiation	Measured
GHI	Global Horizontal Irradiation	Measured
R_f	Surface roughness multiplier in h_c	2.17 for stucco
RH	Relative humidity	Measured 2 m ARL
T_a	Air temperature	Measured 2 m ARL
T_i	Interior air temperature	Prescribed as 23.3 ^{o}C (cooling day) or 21.7 ^{o}C (heating day)
T_p	PV panel temperature	Modeled (Jones and Underwood, 2001)
T_r^{n-1}	Roof temperature at previous time step n-1	
T_1	Temperature at first roof layer	From Crank Nicolson model
α	Roof surface albedo	Measured 0.218
ε_r	Roof emissivity	Assumed 0.95
ε_p	PV emissivity	Assumed 0.95

The model described in section 4 was expanded to simulate the envelope heat flux over a year forced using continuous meteorological observations from the PoSL roof (top of Table 3). Table 4 shows a list of all variables used in the annual roof heat flux model. For the exposed roof, these are (in this order in Eqs. 3 and 4) net shortwave (solar) radiation, incoming longwave radiation, outgoing longwave radiation, convection, conduction into the roof, and change in internal energy (storage). For the PV covered roof, global solar radiation is replaced by diffuse, and incoming longwave radiation comes from both the solar panel and the sky weighted by their relative sky view factors (*SVF*) (Eq. 4).

$$0 \;=\; -(1-\alpha)GHI \;+\; \varepsilon_r\sigma T_r^4 \;-L_{d,sky} \;+\; h_c(T_r - T_a) \;+\; \frac{k}{\frac{1}{2}\Delta x}(T_r - T_1) \;-\frac{\rho c_p \Delta x}{dt}(T_r^{n-1} - T_r) \tag{3}$$

$$0 = -(1-\alpha)DIFF + \varepsilon_r\sigma T_{rs}^4 - (1-SVF)\varepsilon_p\sigma T_p^4 - SVF * L_{d,sky} + h_c(T_{rs} - T_a) +$$

$$\frac{k}{\frac{1}{2}\Delta x}(T_{rs} - T_{1s}) - \frac{\rho c_p \Delta x}{dt}(T_{rs}^{n-1} - T_{rs}) \tag{4}$$

The downwelling longwave radiation from the sky was calculated using (CIMIS 2010)

$$L_{d,sky} = (f\varepsilon_{net} - \varepsilon_r)\sigma T_a^4. \tag{5}$$

The cloud fraction, *f*, is calculated based on the ratio of measured *GHI* to clear sky *GHI* and varies from 0.595 (very cloudy) to 1 (clear). The net emissivity is based on the vapor pressure (e_a, calculated from *RH* and *T*) as $\varepsilon_{net} = 0.34 - 0.14\sqrt{e_a}$. The PV panel temperature (T_p) is needed to calculate $L_{d,pv}$ and was modeled using an energy balance method (Jones and Underwood, 2001).

Model results are most sensitive to the convective heat transfer coefficient (h_c) that was obtained using the DOE-2 convection model (Eqs. 6-8, ASHRAE, 2005b) as a combination of the coefficients for natural convection (h_n) and forced convection over a smooth surface ($h_{c,\,glass}$).

$$h_n = 1.520\sqrt[3]{|T_a - T_r|} \quad \text{(upward heat flow) or} \tag{6a}$$

$$h_n = 0.4958\sqrt[3]{|T_a - T_r|} \quad \text{(downward heat flow)} \tag{6b}$$

$$h_{c,glass} = \sqrt{h_n^2 + [au^b]^2} \tag{7}$$

$$h_c = h_n + R_f\left(h_{c,glass} - h_n\right) \tag{8}$$

The constants *a* and *b* were chosen based on wind tunnel measurements over a smooth surface for the exposed roof and measurements on a 6th floor recessed surface, which experiences a similar drop in wind speeds from the free stream, for the PV covered roof (Palyvos, 2008). h_i = 1.25 W m^{-2} K^{-1} was used for the interior heat transfer coefficient (ASHRAE, 2005b).

Equations 3 and 4 were coupled to the heat conduction model (Section 4) to calculate the heat flux into the building from exterior boundary conditions of T_a, *u*, *RH*, *GHI*, and *DIFF* and interior boundary condition of constant air temperature (T_i). Since Eqs. 3 and 4 are non-linear, Newton's method (Eq. 9) is used to iteratively solve for the roof surface temperature. In Newton's method, T_r at the previous timestep is used as the initial guess (x_i) and Eqs. 3 and 4

and their derivatives (*F* and *F'*) are used iteratively until T_r at the current time step (x_{i+1}) converges.

$$x_{i+1} = x_i - \frac{F(x_i)}{F'(x_i)} \quad (9)$$

The roof heat flux into the building is then calculated from the interior ceiling surface temperature and the assigned interior air temperature by $h_i(T_{32} - T_i)$.

5.2 Validation

The model was validated against the data obtained in the intensive study period. Fig. 7 shows the modeled and measured roof surface temperatures, and Fig. 8 shows the modeled heat flux into the building against the heat flux calculated in Section 4 based on the measured roof temperature. The exposed roof heat flux had a root mean square error (RMSE) of 5.48 W m^{-2} and a mean bias error (MBE) of 4.40 W m^{-2}. The PV covered roof had an RMSE of 2.18 W m^{-2} and a MBE of 1.72 W m^{-2}. Considering the complex environment of a building rooftop the agreement was considered sufficient for validation.

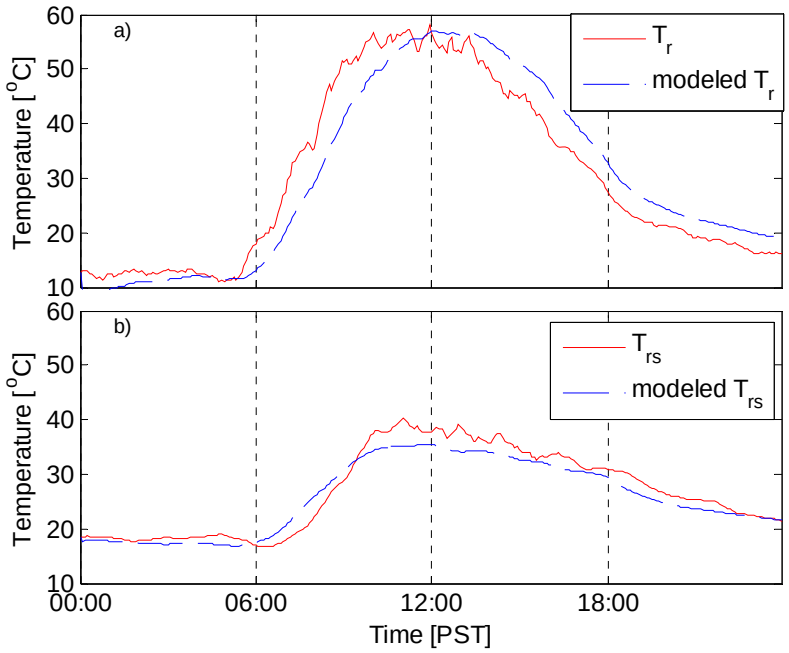

Fig. 7. Measured and modeled roof surface temperature using Eqs. 3 and 4 for a. the exposed roof and b. PV covered roof for April 19, 2009.

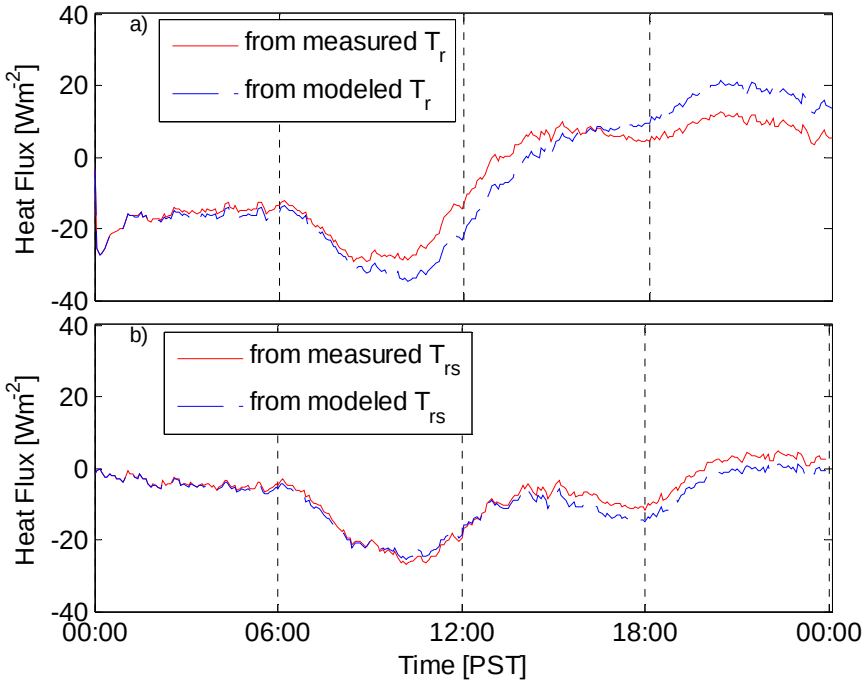

Fig. 8. Heat flux from the ceiling to building air (positive value equals flux into building) computed using the conduction model of Section 4 using the measured T_r (Fig. 6, Section 4) and the modeled T_r (Eqs. 3 and 4) during April 19, 2009 for a) exposed roof and b) PV covered roof.

5.3 Roof cooling load

The roof heat flux contribution to cooling and heating loads is estimated by dividing the days of the year into cooling (average of daily maximum and minimum outside air temperature greater than 18.3 ^{o}C (65 ^{o}F)) and heating (average of daily maximum and minimum temperature less than 18.3 ^{o}C (65 ^{o}F)) days. For cooling (heating) days the total daily net incoming (outgoing) heat flux is assumed to constitute the daily HVAC load related to the roof envelope flux. Based on HVAC set points and hours of operation used in other air-conditioned commercial buildings on campus for cooling days, T_i = 23.3 ^{o}C (74 ^{o}F), and a building schedule of 0800 – 2000 PST are assumed. For the heating days T_i = 21.7 ^{o}C (71 ^{o}F) and a 24 hour building schedule are assumed. The justifications for the building schedules are discussed at the end of Section 5.

The roof cooling and heating load analysis was run by month (Table 5) for all of 2009 which included 155 cooling days and 210 heating days.

Table 5: Mean monthly roof heat flux contributions to cooling and heating loads for 2009. Cooling load is average load during 0800-2000 PST on cooling days. Heating load is average load over the entire heating day. Negative heating load means that the roof heat flows into the building on a heating day. Numbers in italics represent months with 2 or less days of cooling or heating. CDD: cooling degree days. HDD: heating degree days.

Month	CDD/HDD [^{o}C d]	mean cooling load [W m^{-2}]		mean heating load [W m^{-2}]	
		Exposed roof	PV covered	Exposed roof	PV covered
1	33.4/79.4	2.33	0.93	3.40	3.38
2	5.33/120	2.70	1.15	2.06	2.78
3	5.56/118	*5.11*	*4.08*	-0.75	0.70
4	17.4/96.1	12.8	5.79	-1.99	-0.77
5	3.05/38.2	*11.7*	*4.22*	-3.52	-3.43
6	4.44/13.3	8.06	6.48	-4.09	-4.07

7	80.6/0.59	11.4	6.62	*-2.70*	*-5.83*
8	106/0	10.41	7.27	N/A	N/A
9	100/0	9.73	6.31	N/A	N/A
10	30.4/20.6	6.13	3.27	-1.41	-1.16
11	10.1/60.6	4.10	1.71	0.70	1.22
12	3.69/135	*2.25*	*2.68*	3.51	3.12
Total	400/683	8.38	5.21	-0.27	0.16

The maximum cooling load reduction (4.8 W m^{-2}) occurred in July, which was warm and mostly clear. On clear cooling days the benefits of shading are maximized causing a large reduction in cooling load compared to the exposed roof (e.g. Fig. 9). On overcast cooling days the exposed roof is also shaded by clouds so the PV cooling load is similar to the exposed roof cooling load. In June 2009 (a cloudy month) average cooling loads differed by less than 1.6 W m^{-2}.

On heating days the increased longwave radiation from the panel becomes a benefit on all nights (especially clear nights) and (to a lesser extent) on cloudy days. For example, two cloudy heating days in December had a lower heating load for PV during daytime and at night (Fig. 10). On clear heating days the exposed roof has a lower daytime heating load due to the increased solar irradiation. Since only the roof contribution to the heating load was calculated, the solar radiation contribution leads to a negative heating load for many monthly averages, i.e. the roof heat flux is acting to reduce the heating load caused by wall heat fluxes and infiltration. Due to the moderate air temperatures and significant solar irradiation in San Diego winters the annual mean roof heating load is nearly zero for both cases; the heat losses driven by the inside to outside temperature gradient are overcome by heat gain through absorption of solar radiation.

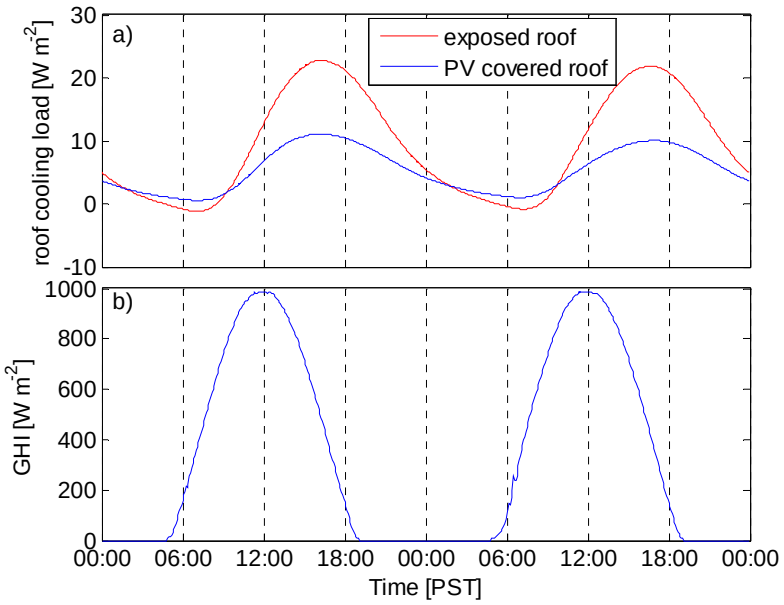

Fig. 9. a. Modeled roof cooling load and b. measured *GHI* on July 12-13, 2009. Hot, cloud-free conditions result in the greatest cooling load savings under the PV array with a mean daily (0800-2000) cooling load of 13.9 W m^{-2} for the exposed roof and 6.19 W m^{-2} for the PV covered roof.

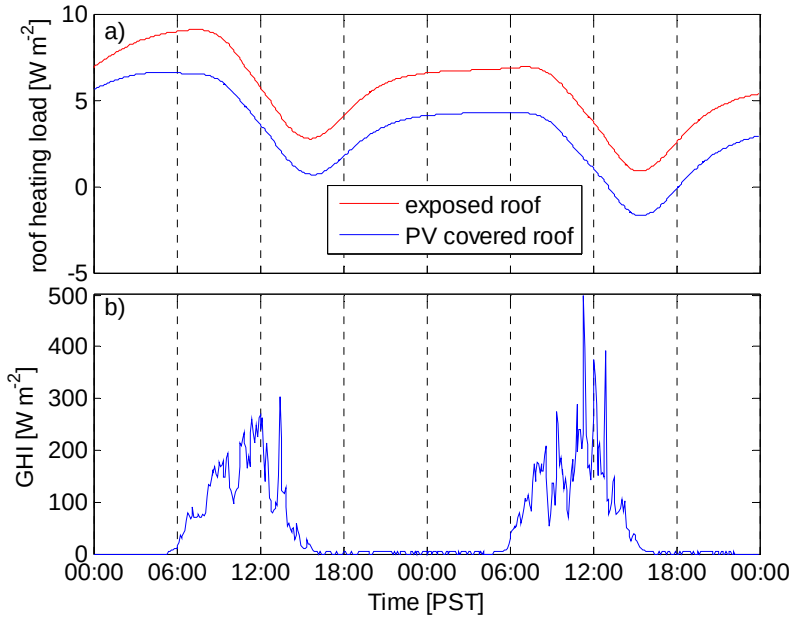

Fig.10. a. Modeled roof heating load and b. measured *GHI* on December 11-12, 2009. Cold and cloudy days result in the greatest reduction in heating load under the PV array, with a mean heating load of 5.96 W m^{-2} for the exposed roof and 4.03 W m^{-2} for the PV covered roof.

The annual cooling or heating load model has several shortcomings. The cooling loads represent only the load necessary to maintain T_i = 23.3^{o}C during the day. The 'startup' load to cool to the desired T_i in the morning at the beginning of HVAC operation is not considered. For cooling load, the effect of ignoring the startup load is small, since the generally cool nights would result in T_i<23.3 ^{o}C at the beginning of HVAC operation. However, for the heating load the 'startup' load can be significant, and was accounted for by using a 24 h building schedule for the heating load. The interior boundary condition does not account for longwave radiative heat exchange between building envelope surfaces. While the absolute results may not be accurate or representative, the differences between the exposed roof and the PV covered roof surface temperature and heat fluxes are considerate correct.

6. Discussion and Conclusions

Careful measurements of the thermal conditions throughout a roof profile on a building partially covered by solar photovoltaic (PV) panels were conducted. Thermal infrared (TIR) imagery demonstrated that ceiling temperatures under the PV arrays were up to 2.5 K lower than under the exposed roof at 1700 PST, a time that lies within the interval of peak energy demand, defined by SDG&E as 1200 – 1800 PST. The daily variability in rooftop surface temperature under the PV array was half that of the exposed roof, indicating a reduction in thermal stresses of the roof structure. The ceiling temperatures under a tilted PV array offset from the roof allowing heat advection were cooler than under a flat array which was mounted flush with the roof. At night with calm winds the conditions reversed and the ceiling under the PV arrays was warmer than the ceiling under the exposed roof, especially for the flush PV array.

Large indoor air and surface temperatures caused the roof heat flux (defined as conductive heat flux from the bottom roof layer to the ceiling) under the tilted PV array to be upward for most of the day. The mean daytime heat flux (1200 – 2000 PST) under the exposed roof in the model was 14.0 W m^{-2} larger than under the tilted PV array. The maximum downward heat flux was 18.7 W m^{-2} for the exposed roof and 7.0 W m^{-2} under the tilted PV array, a 63% reduction due to the PV array. The reduction in heat flux is comparable to the 65% reduction in cooling load shown by the model in (Yang et al., 2001) and the 52% reduction of summertime peak cooling load from the simulation in (Wang et al., 2006). A sensitivity analysis of our results to temperature measurement uncertainty confirms the robustness of the difference in roof heat flux under exposed and PV covered roof (Appendix A).

Expanding the model to utilize internal air temperature (T_i) and outside meteorological conditions (*GHI*, *DIFF*, T_a, *RH*, and *u*) as boundary conditions allowed for the roof heat flux to be modeled for the year 2009 to estimate heating and cooling loads. Total annual cooling load of the PV covered roof decreased 38% to 9.69 kWh m^{-2} from 15.6 kWh m^{-2} for the exposed roof. Considering the total annual PV energy production of 148 kWh m^{-2}, the annual cooling load reduction of 5.91 kWh m^{-2} enhances the annual net energy balance of PV by 4%. The benefits were greatest in July (a warm and sunny month), with a difference in daily cooling load of 57.36 Wh m^{-2} and an average daily PV array electricity production of 570 Wh m^{-2}, resulting in a 10% enhancement of the net energy balance of PV. The difference between PV and exposed roof was dependent on cloud cover, as cloudy days increased the benefits of PV on heating days and decreased the benefits on cooling days. The daytime shading provided by PV becomes a disadvantage on clear heating days as passive heating is reduced compared to the exposed

roof. However, this loss in passive heating is about balanced by a reduction in nighttime radiative heat loss resulting in overall similar heating load for PV covered and exposed roof. The reduction in nighttime heat loss is expected to reduce heating energy use in most regions of the world, especially for residential applications where most heating occurs at night. The tools developed in this study can be used with different meteorological forcing data and roof thermal properties to estimate heating and cooling benefits of PV.

The present study is unique as the impact of tilted and flush PV arrays could be compared against a typical exposed roof at the same roof for a commercial uninhabited building with exposed ceiling and consisting only of the building envelope. Consequently, other factors that often make it difficult to compare different roofing modifications, such as micrometeorological conditions at the site, influence of the surrounding urban environment, occupant behavior, and differences in building thermal properties could be excluded as contributing factors in our study. Nevertheless this is a case study and the results for the impact of PV on the building cooling load may not be generally applicable. Shortcomings of the analysis of the intensive measurements in Section 4 are that (i) the building was unventilated reducing roof cooling load; (ii) the ceiling areas under the different roof sections were thermally coupled through radiative and convective exchange via the building interior and ground slab blunting the thermal differences between exposed and PV covered ceiling; (iii) the corrugated steel on the ceiling may have conducted heat horizontally which is not accounted for in our 1-d model again blunting the thermal differences between exposed and PV covered ceiling. However, all of these shortcomings act to reduce the benefit of shading from the PV panel, so our results could be considered a conservative estimate of PV benefits for this particular building. For a future

study we recommend comparing climate controlled, identical buildings in a neighborhood, one with and one without a PV array.

In addition, the results serve as a potential explanation of the reduction in energy use on hot days found by the California Solar Initiative impact evaluation (ITRON Inc., 2010), which presumably also have the highest roof radiation loading and maximum shading benefit of PV systems. With the exponential growth in rooftop PV, it becomes more important to consider the effect of rooftop PV systems on building HVAC costs. The models for indirect PV effects on cooling load could be used similar to existing roof calculators for insulation improvements and roof albedo increases (e.g. ASHRAE, 2005a; DOE Cool Roof Calculator 2009; EPA Roof Calculator, 2009).

Nomenclature

Term	Description
a	Velocity coefficient in h_c for exposed roof/PV covered roof
b	Velocity exponent in h_c for exposed roof/PV covered roof
c_p	Heat capacity of roof material
e_a	Vapor pressure
f	Cloud fraction
q	Conductive heat flux
h_c	Exterior convective heat transfer coefficient
$h_{c,\ glass}$	Heat transfer coefficient over a smooth surface
h_i	Interior convective heat transfer coefficient
h_n	Natural convection heat transfer coefficient
k	Thermal conductivity of roof material
u	Wind speed
ARL	Above Roof Level
BIPV	Building Integrated PV
CDD	Cooling Degree Days

DIFF	Diffuse irradiation
GHI	Global Horizontal Irradiation
H	Convective (sensible) heat flux
HDD	Heating Degree Days
HVAC	Heating, Ventilating, and Air Conditioning
$L_{d,sky}$	Downwelling longwave radiation from sky
MBE	Mean Bias Error
PoSL	Powell Structural Laboratory
PST	Pacific Standard Time
PV	Photovoltaic
R_f	Surface roughness multiplier in h_c
RH	Relative humidity
RMSE	Root Mean Square Error
SDG&E	San Diego Gas and Electric
SVF	Skyview factor of roof under PV panel
T_a	Air temperature
T_{as}	Air temperature under tilted array
T_c	Ceiling temperature
T_{cs}	Ceiling temperature under tilted array
T_{cflat}	Ceiling temperature under flat array
T_i	Interior air temperature
T_x	Temperature at x^{th} roof layer
T_p	PV panel temperature
T_r	Roof surface temperature
T_{rs}	Roof surface temperature under tilted array
T_r^{n-1}	Roof temperature at previous time step
TIR	Thermal Infrared
α	Roof surface albedo
ε_{net}	Net emissivity of air
ε_r	Roof emissivity
ε_p	PV emissivity
ρ	Density of roof material
σ	Stefan-Boltzmann constant
Δx	Discretized spacing of roof layers

Appendix A: Sensitivity Analysis

The sensitivity of the heat flux calculation to the surface temperatures was analyzed by varying the offset between roof surface temperatures T_{rs} and T_r and the ceiling temperatures acquired

by the TIR camera (T_c). Figure 12 shows that offsetting exposed roof and PV covered roof measurements has a small effect on reduction in peak heat flux and difference in mean daytime heat flux. Offsetting T_{rs} and T_r within a +- 0.5 ^{o}C window (a typical uncertainty of a thermistor) results in a range of 55% - 69% reduction in peak heat flux and a mean daytime heat flux difference of 12.2 – 15.9 W m^{-2}. These narrow ranges show that our heat flux results are robust.

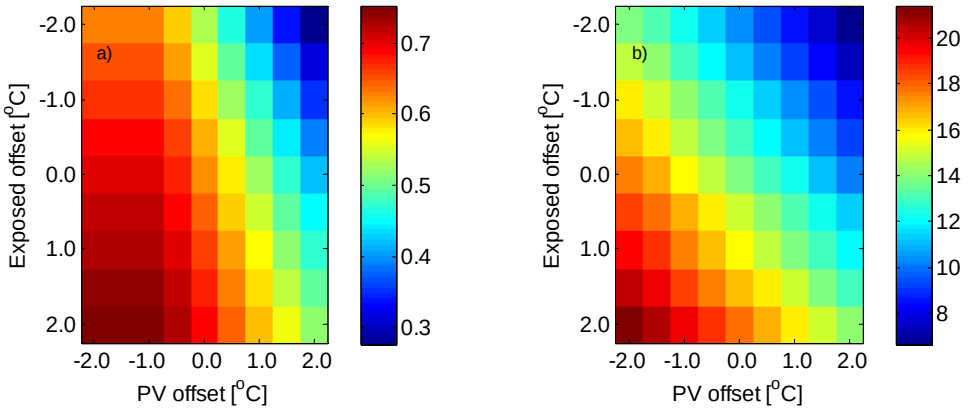

Fig. 11: Sensitivity of a. reduction of peak roof heat flux [%/100] and b. difference in mean daytime (1200 - 2000 PST) heat flux [W m^{-2}] to offsets in exposed roof (T_r) and PV roof (T_{rs}) surface temperatures (see Fig. 6c for a plot of this heat flux for the exposed roof and PV roof).

Appendix B: Extension of conductive heat flux analysis to include flush PV array

In a manner similar to the derivation of sol-air or environmental temperatures outdoors, the heat flux into the building air can be simplified into some overall indoor heat transfer coefficient h_i times the difference in the ceiling surface temperature T_c and some internal environmental temperature T_{ie}

$$q = h_i(T_c - T_{ie}) \quad \text{(A.1)}$$

Knowing q and T_c for both the exposed roof case and the tilted PV array (section 4) at each time step allows solving for h_i and T_{ie} for each time step using the linear system of Eq. A.1. These can in turn be used to solve for the heat flux under the flush array given the ceiling temperature. The daytime results of this analysis (Fig.12) show that the mean daytime heat flux (1200-2000 PST) is 7.25 W m^{-2} less than under the exposed roof and 6.78 W m^{-2} greater than that under the tilted array.

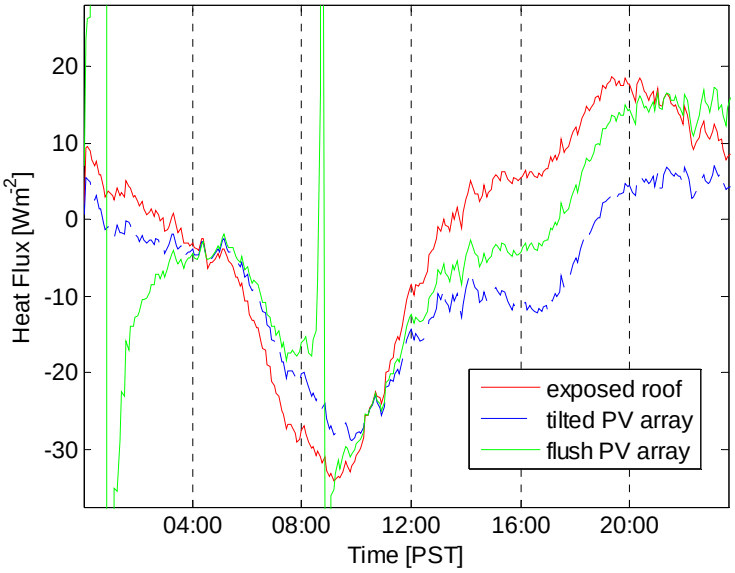

Fig. 12. Heat flux through the bottom roof layer (section 4., Eq. 2) for all three roof types. The solution goes to infinity, however, when the $T_{c,exposed}$ equals $T_{c,pv}$ or q_{PV} equals $q_{exposed}$ which occurs around 0100 and 0900 PST.

Acknowledgements

Anthony Dominguez was funded by the NASA graduate student researchers program. Kleissl acknowledges funding from a NSF CAREER award and the Hellman foundation. The following UCSD undergraduate students were instrumental in the data collection: Avneet Singh, Kevin

Chivatakarn, Thomas Minor, Jeremiah Farinella. We thank Ronnen Levinson for contributing his expertise and the Powell Structures Laboratory building staff, especially Andrew Gunthardt, for being supportive of our work and allowing access to the building for the measurements.

References

H. Akbari, S. Bretz, D.M. Kurn, J. Hanford. Peak power and cooling energy savings of high-albedo roofs, *Energy and Buildings 25* (1997a) 117-126

H. Akbari, D.M. Kurn, S.E. Bretz, J.W. Hanford, Peak power and cooling energy savings of shade trees, *Energy and Buildings 25* (1997b) 139-148

H. Akbari and L. Rainer, Measured Energy Savings from the Application of Reflective Roofs in 3 AT&T Regeneration Buildings (2000). *Lawrence Berkeley National Laboratory.* Paper LBNL-47075.

ASHRAE (2005a), Cooling Load Components, Microsoft Excel spreadsheet calculator available through the ASHRAE bookstore.

ASHRAE Toolkit Chapter 3, Exterior Heat Balance (2005b).

CIMIS evapotranspiration model, http://wwwcimis.water.ca.gov/cimis/infoEtoPmEquation.jsp, accessed September 25, 2010.

Department of Energy (DOE) Cool Roof Calculator, http://www.ornl.gov/sci/roofs%2Bwalls/facts/CoolCalcEnergy.htm, accessed Nov 16, 2009

Environmental Protection Agency (EPA), 2009, http://roofcalc.com/RoofCalcBuildingInput.aspx, accessed Nov 16, 2009

Itron Inc., CPUC California Solar Initiative 2009 Impact Evaluation, 2010, http://www.cpuc.ca.gov/NR/rdonlyres/70B3F447-ADF5-48D3-8DF0-5DCE0E9DD09E/0/2009_CSI_Impact_Report.pdf, accessed July 13, 2010.

A.D. Jones and C.P. Underwood, A thermal model for photovoltaic systems, *Solar Energy*, Vol. 70:4 (2001) 349 -359.

J.A. Palyvos, A survey of wind convection coefficient correlations for building envelope energy systems' modeling, *Applied Thermal Engineering* Vol. 28:8-9 (2008) 801-808.

D.S. Parker and S.F. Barkaszi, Roof solar reflectance and cooling energy use: field research results from Florida, *Energy and Buildings 25* (1997) 105-115

J.R. Simpson, E.G. McPherson, The effects of roof albedo modification on cooling loads of scale model residences in Tucson, Arizona, *Energy and Buildings 25* (1997) 127-137

Thermal Properties of Concrete, http://people.bath.ac.uk/absmaw/BEnv1/properties.pdf, accessed January 22, 2010.

W. Tian, Y. Wang, Y. Xie, D. Wu, L. Zhu and J. Ren, Effect of building integrated photovoltaics on microclimate of urban canopy layer, *Building and Environment 42* (2007) 1891-1901

C.P. Underwood and F.W.H. Yik, Modeling Methods for Energy in Buildings, *Blackwell Publishing Ltd* (2004)

Y. Wang, W. Tian, J. Ren, L. Zhu, and Q. Wang, Influence of a building's integrated-photovoltaics on heating and cooling loads, *Applied Energy 84* (2006) 983-1003

H.X. Yang, J. Burnett, Z. Zhu and L. Lu, A simulation study on the energy performance of photovoltaic roofs, *ASHRAE Trans 107* (2001) (2), 129–135